

Three-dimensional vortex structure of a fast rotating Bose-Einstein condensate with harmonic-plus-quartic confinement

Ionut Danaila

Laboratoire Jacques-Louis Lions, Université Paris 6, 175 rue du Chevaleret, 75013 Paris, France.

(Dated: October 31, 2018)

We address the challenging proposition of using real experimental parameters in a three-dimensional (3D) numerical simulation of fast rotating Bose-Einstein condensates. We simulate recent experiments [V. Bretin, S. Stock, Y. Seurin and J. Dalibard, Phys. Rev. Lett. 92, 050403 (2004); S. Stock, V. Bretin, S. Stock, F. Chevy and J. Dalibard, Europhys. Lett. 65, 594 (2004)] using an anharmonic (quadratic-plus-quartic) confining potential to reach rotation frequencies (Ω) above the trap frequency (ω_{\perp}). Our numerical results are obtained by propagating the 3D Gross-Pitaevskii equation in imaginary time. For $\Omega \leq \omega_{\perp}$, we obtain an equilibrium vortex lattice similar (as the size and number of vortices) to experimental observations. For $\Omega > \omega_{\perp}$ we observe the evolution of the vortex lattice into an array of vortices with a central hole. Since this evolution was not visible in experiments, we investigate the 3D structure of vortex configurations and 3D effects on vortex contrast. Numerical data are also compared to recent theory [D. E. Sheehy and L. Radzihovsky, Phys. Rev. A 70, 063620 (2004)] describing vortex lattice inhomogeneities and a remarkably good agreement is found.

PACS numbers: 03.75.Fi,02.70.-c

I. INTRODUCTION

In recent years, several experimental studies provided evidence for the existence of quantized vortices in rotating Bose-Einstein condensates (BEC's) [1, 2, 3, 4, 5, 6, 7]. The condensate is typically confined by a harmonic (quadratic) potential with transverse frequency ω_{\perp} and starts to nucleate vortices when the rotation frequency Ω exceeds a critical value Ω_c . For increasing $\Omega > \Omega_c$, more and more vortices appear and arrange themselves into a regular triangular (Abrikosov) lattice.

The fast rotation regime, corresponding to $\Omega \gtrsim \omega_{\perp}$, is particularly interesting to explore since a rich variety of scenarios are theoretically predicted: formation of giant (multi-quantum) vortices, vortex lattice melting or quantum Hall effects. This regime is experimentally delicate to investigate [8] since for $\Omega = \omega_{\perp}$ the centrifugal force compensates the trapping force and the confinement vanishes. Using evaporative spin up, the Boulder group has recently created condensates with rotation frequencies of the order of $0.99\omega_{\perp}$ and studied the properties of the vortex lattice in the lowest Landau level [9, 10, 11].

Another experimental approach to reach the fast rotation regime was explored by the École Normale Supérieure (ENS) group [12, 13, 14]. It consists in modifying the quadratic trapping potential by superimposing a blue detuned laser beam to the magnetic trap holding the atoms. The resulting *harmonic-plus-Gaussian* potential removes the singularity at the limit $\Omega = \omega_{\perp}$ and allows to reach rotation rates up to $\Omega \simeq 1.05\omega_{\perp}$. The trapping potential used in these experiments can be well approximated by a *quadratic-plus-quartic* form, which has been extensively studied lately [15, 16, 17, 18, 19, 20, 21, 22, 23, 24]. Different transitions involving a rich variety of vortex states are theoretically predicted when Ω is increased: from a dense vortex

lattice to an array of singly quantized vortices with a central hole and, finally, to a giant (multiquantum) vortex or directly from a vortex lattice to a giant vortex.

For the highest rotation rates reached in experiments, neither giant vortices nor vortex arrays with hole were clearly observed [12, 13]. In exchange, a dramatic change in the appearance of the condensate was reported: the vortices are less visible even though the gas remains ultracold and in fast rotation. The most likely explanation for this intriguing behavior was related to the transient character of the observed states leading to a fragile vortex lattice dominated by three-dimensional (3D) effects (vortices appear to have some excitation or bending leading to poor optical contrast).

Since such effects are not trackable with previous (2D) numerical approaches, the purpose of the present contribution is to investigate the 3D structure of such condensates by numerically generate the corresponding Gross-Pitaevskii (GP) wave function. This is not without its challenges, since the description of a prolate (cigar-shaped) condensate with a large number of vortices (exceeding 100) requires very high spatial resolution and accurate integration schemes. Computations become very expensive at high rotation frequencies, which explains why such 3D simulations are not, to the author's knowledge, currently available in the open literature.

The numerically generated 3D condensates can be seen in Fig. 1. For increasing rotation frequencies, the vortex lattice evolves to a vortex array with a hole, which confirms the scenario theoretically predicted [15, 16, 19, 20] and also observed in 2D simulations [18, 24]. Since such transition was not observed in experiments, we qualitatively analyze the obtained vortex states, with a particular emphasis on the 3D features of vortex merging leading to a central hole in the condensate.

Our analysis is then extended to quantitative compar-

isons to experiments and theoretical predictions. We first check that physical parameters (size, chemical potential) of numerical condensates correspond well to available experimental ones. We show in particular that the rotation frequencies reached in experiments were not enough high to obtain an annular condensate. We also measure from simulations the intervortex spacing and compare the numerical results to recent theory of Sheehy and Radzihovsky [26, 27] describing vortex lattice inhomogeneities. A remarkably good agreement is found. Finally, we discuss how 3D structure of vortices can affect optical contrast of transient states observed in experiments.

II. PHYSICAL PARAMETERS AND NUMERICAL APPROACH

We consider a BEC of N atoms confined by the trapping potential V and rotating along the z axis at angular velocity Ω . In the experiments at ENS [12, 13, 14], $N = 3 \times 10^5$ atoms and the trapping potential can be written as the superposition of the harmonic potential V_h created by the magnetic trap and the potential $U(r)$ introduced by the laser beam propagating along the z axis:

$$V(r, z) = V_h(r, z) + U(r), \quad (1)$$

with $r = \sqrt{x^2 + y^2}$ and

$$V_h = \frac{1}{2}m(\omega_{\perp}^{(0)})^2 r^2 + \frac{1}{2}m\omega_z^2 z^2, \quad U(r) = U_0 e^{-2r^2/w^2}. \quad (2)$$

The trapping frequencies are $\omega_{\perp}^{(0)} = 2\pi \times 75.5$ Hz and $\omega_z = 2\pi \times 11$ Hz, resulting in a cigar-shaped condensate. The laser waist is $w = 25$ μm and the amplitude of the laser beam is $U_0 = k_B \times 90$ nK.

For r/w sufficiently small, the potential $V(r)$ can be approximated by:

$$V_1 = \left[\frac{1}{2}m(\omega_{\perp}^{(0)})^2 - \frac{2U_0}{w^2} \right] r^2 + \frac{2U_0}{w^4} r^4 + \frac{1}{2}m\omega_z^2 z^2. \quad (3)$$

For this *quadratic-plus-quartic* potential, the transverse trapping frequency is decreased to $\omega_{\perp} = 2\pi \times 65.6$ Hz. Since the amplitude U_0 of the laser beam is low in experiments, the quadratic part of the potential V_1 remains positive (repulsive interactions) and the quartic part is very small. It is interesting to note that a stronger amplitude U_0 could generate a *quartic-minus-quadratic* potential, which was theoretically studied in Refs. [20, 22, 25].

The numerical results presented in this paper were obtained using a *quadratic-plus-quartic* potential (Eq. 3), for which extensive theoretical studies are available [15, 16, 17, 18, 19, 20, 21, 22, 23, 24]. Numerical simulations using the *quadratic-plus-Gaussian* original potential (Eq. 2) showed the same qualitative evolution of the vortex configuration as in Fig. 1, with a transition to a vortex array with hole for a slightly lower rotation frequency.

As a numerical approach, we compute the macroscopic wave-function $\psi(x, y, z)$ by propagating the three-dimensional Gross-Pitaevskii (GP) equation in imaginary time by the numerical method used in Refs. [22, 28, 29]. After rescaling the GP equation as in Ref. [30], a hybrid Runge-Kutta-Crank-Nicolson scheme is used for the time integration and a sixth-order compact finite difference scheme for the space discretization.

As initial condition we generally use a vortex-free density distribution following the Thomas-Fermi (TF) law:

$$\rho_{\text{TF}}(r, z) = \frac{m}{4\pi\hbar^2 a_s} \left(\mu - V_1(r, z) + \frac{1}{2}m\Omega^2 r^2 \right), \quad (4)$$

where $a_s = 5.2$ nm is the scattering length and μ the chemical potential given by the constraint $\int d^3r \rho_{\text{TF}} = N$. For the *quadratic-plus-quartic* trapping potential V_1 , an exact analytical form for μ can be derived [15] depending on the value of Ω which dictates the shape of the condensate (with or without a hole). The maximum transverse radius R_{\perp} and longitudinal half-length R_z can be then calculated from Eq. (4) in order to estimate the dimensions of the rectangular computational domain. For high Ω (when the condensate is nearly spherical and more than 100 vortices are present), up to $240 \times 240 \times 240$ grid points are used to compute equilibrium states.

The post-processing of the results follows the experimental approach [11, 12] (with the difference that the radial expansion after the time of flight is not numerically simulated). The numerical 3D wave-function is converted to an atomic density $\rho(x, y, z) = |\psi(x, y, z)|^2$ and integrated along the rotation (z) axis. The resulting 2D-density $\bar{\rho}^2(x, y)$ (isocontours are displayed in Fig. 1, last row of images) will be used in the following for comparison to experiments and theory.

III. DESCRIPTION OF THE RESULTS

The evolution of the 3D structure of the condensate with increasing Ω can be seen in Fig. 1. We start with a qualitative description of vortex configurations. The obtained results will be then analyzed quantitatively and compared to available experimental and theoretical values. All quantitative parameters discussed in this paper are summarized in table I.

A. Vortex configurations

For rotation frequencies below ω_{\perp} ($\Omega/(2\pi) = 60$ and 64) the condensate has the usual prolate shape (see Fig. 1, first two columns). Vortices near the center of the condensate are straight and form a regular triangular lattice. Vortices located near $r = R_{\perp}$ are bending, reaching the surface of the condensate using the shortest path. These outer vortices are not symmetrically arranged and have different lengths. It is interesting to note that for these

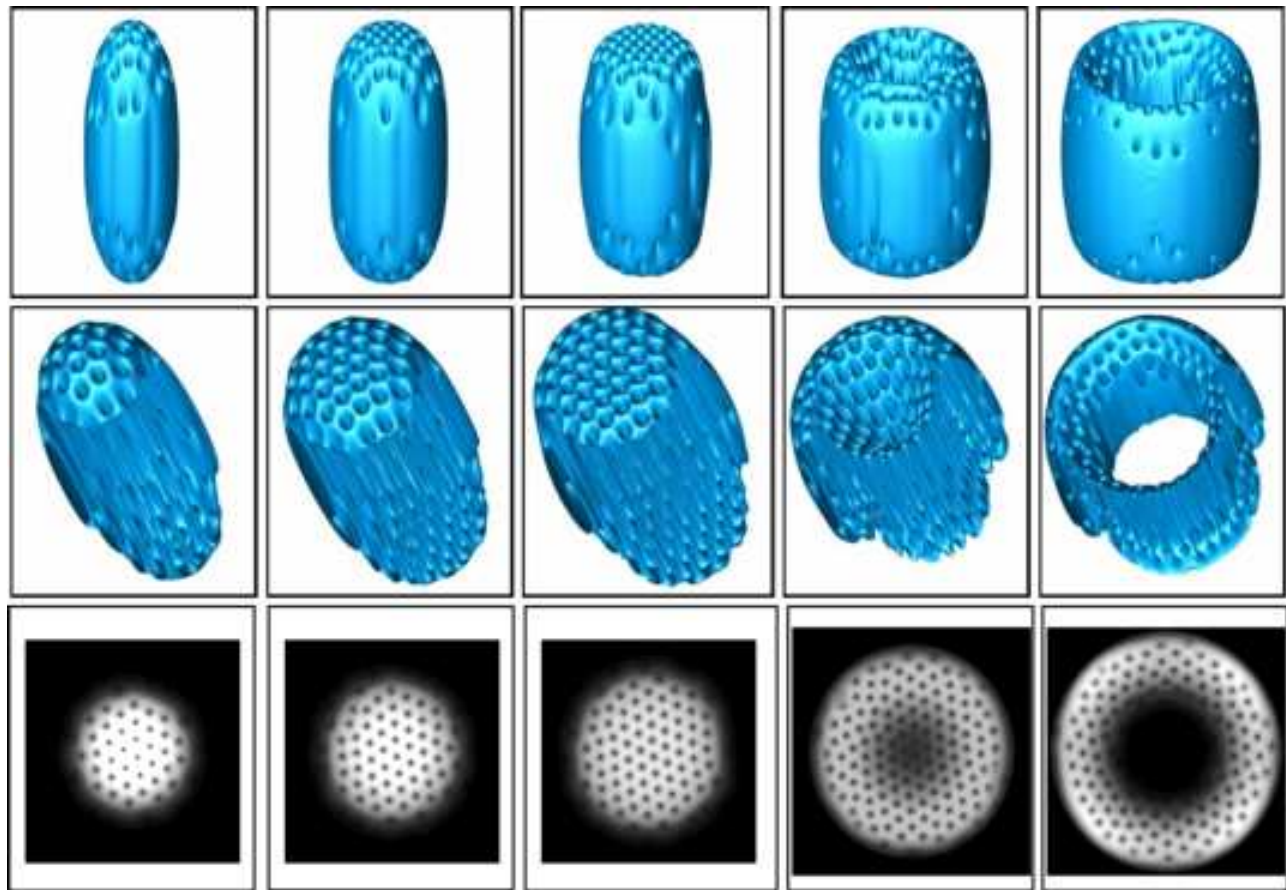


FIG. 1: (Color online) Numerically generated condensates obtained using a *quadratic+quartic* trapping potential with the parameters corresponding to experiments of [12, 13]. Each column corresponds to a value of the rotation frequency - from left to right: $\Omega/2\pi = 60, 64, 66, 70.6, 73$ (respectively, $\Omega/\omega_{\perp} = 0.92, 0.98, 1.01, 1.08, 1.11$). Three-dimensional views of the vortex lattice identified by means of iso-surfaces of low atomic-density (first two rows) and contours of density integrated along the rotation (z) axis. Note that the formation of the hole in the condensate is not complete for $\Omega/2\pi = 70.6$ and we still distinguish individual singly-quantized vortices in the center (see also Fig. 2 for a detailed picture of this configuration).

$\Omega/(2\pi)$	60	64	66	70.6	73
Ω/ω_{\perp}	0.92	0.98	1.01	1.08	1.11
$R_{\perp} [\mu\text{m}]$	10.4	12.2	13.2	17.2	19.2
$R_z [\mu\text{m}]$	29.0	25.4	22.5	20.1	18.6
N_v	37	51	62	126	113
$L_z [\text{units of } \hbar]$	17.4	28.5	39.1	122.6	239.1
r_v/ξ	2.15	1.84	1.65	1.36	1.76

TABLE I: Summary of the characteristics of numerically generated condensates: (maximum) transverse radius R_{\perp} and longitudinal half-length R_z ; number of vortices N_v and angular momentum $L_z = i \int d^3r \bar{\psi} (y \partial \psi / \partial x - x \partial \psi / \partial y)$; scaling constant for the ratio between vortex-core radius r_v and healing length ξ [obtained from integrated density $\bar{\rho}^z(x, y)$].

two values of Ω , the number of vortices N_v we find numerically ($N_v = 37$ and 51) is very close to that visible in experimental pictures [12] ($N_v^{exp} = 30$ and 52).

Starting with $\Omega/(2\pi) = 66$ ($\Omega/\omega_{\perp} = 1.01$), the exper-

imental pictures show a lack of contrast for entire zones of the vortex lattice. Vortices are less visible and do not allow a proper estimation of the rotation frequency from vortex surface density. Numerical condensate for this rotation frequency (Fig. 1, third column) display a well-defined triangular vortex lattice. Most of the vortices are straight and join the top and bottom ends of the condensate which are almost flat. This particular shape of the condensate corresponds well to that predicted from the TF law (4). Indeed, for $\Omega = \omega_{\perp}$, the density distribution $\rho_{\text{TF}}(r, z)$ depends only on the quartic part of the trapping potential V_1 and the surface of the condensate defined as $\{\rho_{\text{TF}} = 0\}$ is flat near the rotation z axis.

For rotation frequencies exceeding ω_{\perp} , experimental condensate exhibits a local minimum in the central density, but the theoretically predicted [15, 18] transition to a vortex lattice with a hole (annular condensate) is not experimentally reported. This is the case in our simulations (Fig. 1). The rotation frequency corresponding to this transition is found to be $\Omega_h/(2\pi) = 71$, a value close to the TF prediction $\Omega_h^{\text{TF}}/(2\pi) = 70$. These val-

ues are already larger than those attained in experiments ($\Omega/(2\pi) < 69$), which can simply explain why the hole was not experimentally observed.

The numerically generated condensates before and after transition to an annular condensate are shown in Fig. 1 (last two columns of images). For $\Omega/(2\pi) = 70.6$, the central hole is not yet formed since the top and bottom depletions have not merged. At the center of the condensate, the density is very low but not zero, and we can still distinguish individual vortices from isocontours of the density integrated along the z axis (Fig. 1). Since the contrast in this last image is low near the center, we show details of the vortices near the rotation axis in Fig. 2. In the center there are three vortices with larger cores that start to reconnect at the top and bottom of the condensate. This merging process is highly three-dimensional and will finally lead to the formation of a central hole for higher Ω .

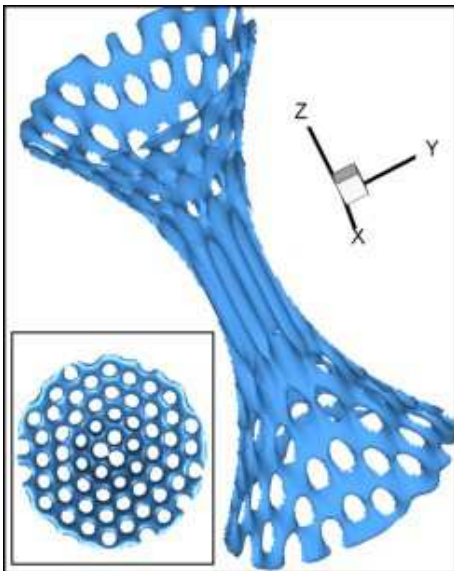


FIG. 2: (Color online) Details of the vortex configuration for $\Omega/(2\pi) = 70.6$. Vortices near the rotation axis are isolated, showing the merging process that will finally lead to the formation of a central hole. Insert: top view of the same configuration.

The structure of the condensate is completely different for $\Omega/(2\pi) = 73$ (last column of images in Fig. 1). The condensate is nearly spherical, with a large central hole surrounded by three concentric circles of singly quantized vortices. Most of the 113 identified vortices are bent, reaching either inner or outer faces of the condensate. Since convergence for this case is particularly slow (two weeks of computational time is necessary using a PC workstation), we did not explore cases for higher Ω . For the considered parameters, a second transition to a configuration with a pure giant vortex (without singly quantized vortices in the annular region) may occur at very high rotation frequencies [24] that are not numerically affordable in 3D.

B. Vortex lattice inhomogeneity

We now turn on more quantitative analysis of numerical results. Before analyzing the characteristics of the vortex lattice, we first check that the dimensions of the numerically generated condensates correspond well to experimental ones. The density $\bar{\rho}^z$ is integrated along the azimuthal direction θ to get the radial density profile $\bar{\rho}^{z,\theta}(r)$. This profile is fitted to the Thomas-Fermi distribution (4), taking the chemical potential μ and the rotation frequency Ω as adjustable parameters. The theory fit value of Ω is within 1% of the value of Ω for which the computation was done.

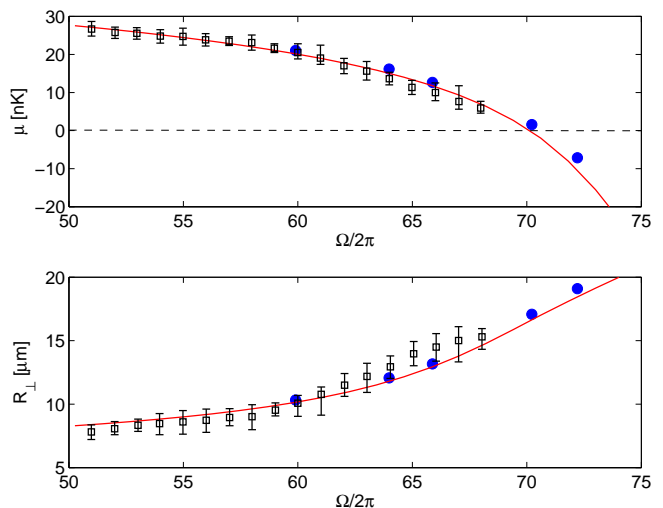


FIG. 3: (Color online) Chemical potential (μ) and maximum transverse radius of the condensate (R_{\perp}) as functions of the rotation frequency. Experimental measurements from Ref. [14] (squares), numerical results (circles) and Thomas-Fermi theoretical prediction (solid line).

The resulting chemical potential μ and the transverse radius R_{\perp} (which is the maximum radius for the condensate with hole) are compared in Fig. 3 to experimental values from Ref. [14] and Thomas-Fermi approximation (4). For the experimentally available range of rotation frequencies, numerical results are in good agreement with experimental and theoretical values. For values of Ω not available experimentally, numerical results follow the TF prediction. In particular, the numerical value $\Omega_h/(2\pi) = 71$ for which the central hole first appears in the condensate (corresponding to a chemical potential $\mu = 0$) is well predicted by the TF law ($\Omega_h^{\text{TF}}/(2\pi) = 70$).

We continue our dimensional analysis by extracting the characteristics of the vortex lattice: namely the intervortex spacing b_v and the vortex core size r_v . We follow a similar post-processing procedure as in Ref. [11]. Using the integrated (along z) density field $\bar{\rho}^z(r, \theta)$, we identify vortex centers by 2D searching of local minima. Resulting points are checked to correspond to vortices visible in Fig. 1 (last row of images). Assuming a triangular lattice

structure, we select vortices for which the six nearest vortex neighbors form a hexagonal pattern. Only for such vortices (i.e. vortices close to R_{\perp} are discarded), is the intervortex spacing b_v measured by averaging the distance from the vortex center to the centers of the six neighbors. The vortex core radius r_v is measured as follows: for a given vortex located at (r_0, θ_0) , the density profile $\bar{\rho}_v^z(r)$ along the radius passing through the center of the vortex is extracted from the 2D field $\bar{\rho}^z$; by subtracting the integrated TF density profile $\bar{\rho}_{\text{TF}}^z(r)$ [corresponding to Eq. 4 integrated along z], we obtain a vortex-core residual that is fitted with a Gaussian profile:

$$\bar{\rho}_{\text{TF}}^z(r) - \bar{\rho}_v^z(r) = A \exp \left[-\frac{1}{2}(r - r_0)^2 / r_v^2 \right]. \quad (5)$$

The amplitude A is used to define the vortex contrast [11] as $A/\bar{\rho}_{\text{TF}}^z(r_0)$, i.e. the ratio between the "missing" column density at vortex center r_0 and the corresponding TF value. Only vortices with a contrast greater than 0.7 are considered to compute core radii r_v .

Figure 4 shows the variation of r_v and b_v as functions of the non-dimensional radius r/R_{\perp} . Values are given in μm and rotation frequencies $\Omega/\omega_{\perp} \leq 1.01$ are considered (condensates without hole). As expected [11, 15], the core radius r_v scales with healing length, defined from the TF density fit $\xi(r) = [8\pi a_s \bar{\rho}_{\text{TF}}^z(r)]^{-1/2}$. The scaling constant (also summarized in Tab. I) decreases with Ω , with values comparable to those found in Ref. [11] for a harmonic trapping potential. We recall that the values presented here correspond to a post-processing for r_v using integrated density $\bar{\rho}^z$, as in experiments. A similar post-processing using the 2D density field ρ extracted from the 3D simulation at $z = 0$, revealed scaling constants for r_v/ξ of order of 1 (more precisely, $r_v/\xi \approx 0.98, 0.93, 0.86$ for, respectively, $\Omega/2\pi = 60, 64, 66$).

The calculated intervortex spacing b_v is compared in Fig. 4 to recent theory of Sheehy and Radzihovsky [26, 27]. They expressed the vortex density $n_v(r)$ as a function of the local superfluid density $\rho_s(r)$:

$$n_v(r) = \frac{\Omega m}{\pi \hbar} + \ln[\hbar / (2.718 m \Omega \xi_v^2)] \nabla^2 [\ln(\rho_s(r))]. \quad (6)$$

The second term in (6) is a small correction to the vortex density for a uniform vortex distribution corresponding to a rigid-body rotation $n_{v0} = (\Omega m)/(\pi \hbar)$. The vortex density n_v can be converted to intervortex spacing by:

$$b_v(r) = \sqrt{2/(3^{1/2} n_v(r))}. \quad (7)$$

Numerical results are compared to theoretical predictions using in Eq. 6 the TF fit for the integrated density profile ($\rho_s(r) = \bar{\rho}_{\text{TF}}^z(r)$) and the characteristic length for the vortex-core ξ_v defined as [26] $\xi_v = \hbar/(m\omega_{\perp} R_{\perp})$. The agreement is remarkably good. For $\Omega/2\pi \leq 64$, the density profile is close to an inverted parabola (the influence of the quartic term being small) and b_v is monotonically increasing with r . Similar results were reported

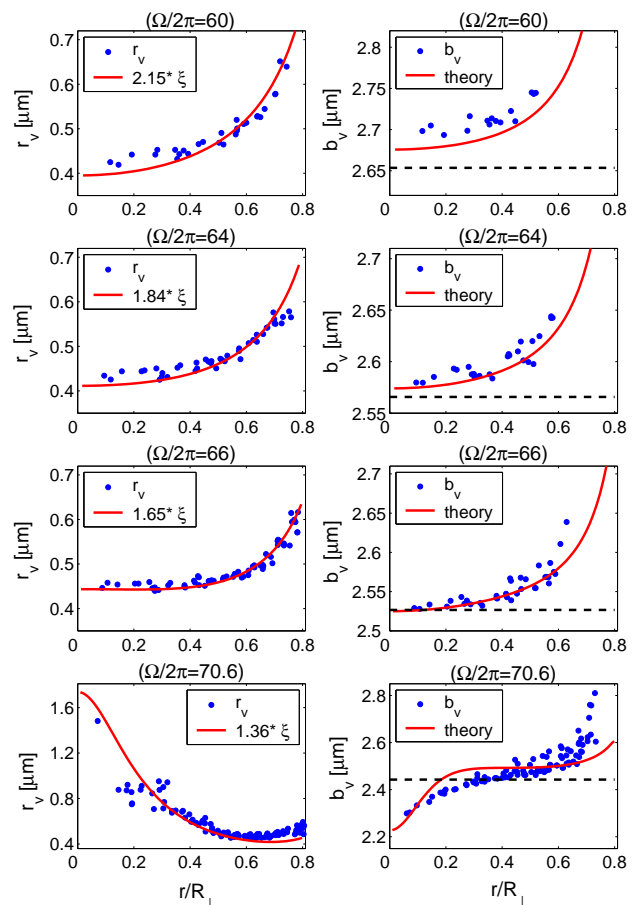


FIG. 4: (Color online) Variation of vortex core radius r_v and intervortex spacing b_v (values in μm) as functions of the non-dimensional radius r/R_{\perp} . For each plot, the value of the rotation frequency ($\Omega/2\pi$) is indicated. In plots displaying r_v , solid line represents the variation of the healing length ξ , scaled by a constant indicated in the legend. Variation of b_v is compared to theory prediction of Sheehy and Radzihovsky [26, 27] (solid line) and the estimation assuming a uniform (rigid-body) vortex distribution (dashed line).

for a harmonic trapping potential [11]. As expected, the estimation using the rigid-body rotation assumption (dashed line in the plot) becomes better with increasing Ω (the lattice becomes denser). For $\Omega/2\pi = 70.6$, the density profile has a Mexican-hat structure and vortices are constrained to agglomerate towards the center, where density is small. The intervortex spacing is small near the center and increases to the rigid-body value near $r/R_{\perp} \simeq 0.5$ where the density is maximum. The theory nicely illustrates this complex dependence of b_v on the radial position.

IV. DISCUSSION AND CONCLUSION

We have presented in this paper three-dimensional numerical results for a fast-rotating BEC trapped in

quadratic-plus-quartic potential corresponding to experiments at ENS [12, 13]. The obtained vortex configurations show a transition from a dense vortex lattice to a vortex array with a central hole at a critical rotation frequency $\Omega_h/(2\pi) = 71$. This result confirms theoretical and 2D numerical results [15, 18, 24] and goes beyond experimental observations, since experiments failed to reach rotation frequencies close to Ω_h .

Our results also support the assumption [12] that vortices are less visible in experiments for $\Omega/(2\pi) \geq 66$ because of the fragility of the vortex lattice which becomes dominated by 3D-effects, such as vortex bending. In order to illustrate this statement it is worth describing how the condensate evolves in the "imaginary" time (i.e. how it relaxes to an equilibrium state).

The imaginary-time evolution of the condensate looks similar to a real-time evolution. When suddenly increasing Ω , new vortices are generated at the border of the condensate and enter the condensate. In the first stages of the computation, 3D vortex lines are strongly distorted, giving a *spaghetti* image of the lattice. Close to equilibrium, vortices become straight in their central part and arrange themselves in a more and more regular lattice. Convergence is particularly slow at the end of the computation when the position and shape of vortices evolve very slowly. Convergence is considered when the energy remains constant (relative fluctuations less than 10^{-6}) for a relatively long time to be sure that a stable state was obtained. The convergence time is much longer (roughly by a factor of 2) for values of the rotation frequency exceeding ω_{\perp} .

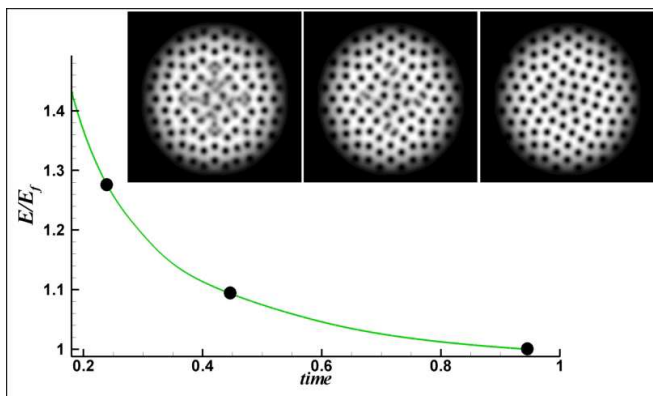


FIG. 5: Example of energy decrease during the propagation of 3D Gross-Pitaevskii equation in imaginary time. Simulation for $\Omega/(2\pi) = 66$, using the quadratic-plus-Gaussian trapping potential (2). Energy is normalized by the equilibrium (final) value E_f . Inserts show iso-contours of the integrated (along z) density corresponding to three successive time instants represented on the energy curve.

An example of intermediate states of the condensate before reaching a converged equilibrium state is displayed in Fig. 5. The simulation corresponds to a quadratic-plus-Gaussian trapping potential (2), (closer to the experimental one) and a vortex configuration without hole. Transient states look closer to experimental pictures than the equilibrium states presented in Fig. 1. Three-dimensional exploration of the condensate reveals that vortices which are less visible have distorted structures which diminish the contrast in an integrated view along the z axis. These effects are stronger for condensates displaying a central depletion; even for equilibrium states of such condensates, it is difficult to distinguish individual vortices in the center, as can be seen in Fig. 1 for $\Omega/(2\pi) = 70.6$. This confirms the hypothesis [12] of the fragility of the experimental vortex lattice for high rotation frequencies: for transient states, 3D vortex lines have some excitations leading to a poor optical contrast. It is possible that the very low temperature in experiments slows down the dissipative process allowing only the observation of transient states dominated by 3D effects. But is not to be excluded that a thermal excitation may be at the origin of the vortex-line bending responsible for low optical contrast and, therefore, increasing the temperature in experiments is not a solution to improve vortex lattice contrast.

Our simulations also offer a detailed 3D picture of vortex configurations that is not available from experiments and 2D simulations. In particular, the vortex merging leading to the formation of the central hole in a condensate is proved to be highly three-dimensional. Quantitative measurements of the intervortex spacing give a new validation of the theoretical study of Sheehy and Radzihovsky [26, 27] predicting vortex lattice inhomogeneity from local density profile. An interesting question remaining for future numerical investigations is whether or not the condensate trapped in a quadratic-plus-quartic potential enters the lowest Landau level regime for $\Omega \simeq \Omega_h$.

Acknowledgments: I am grateful to J. Dalibard and S. Stock for helpful comments on the manuscript and for allowing me to use their experimental data. A. Aftalion and V. Bretin are also acknowledged for useful discussions.

[1] M. R. Matthews, B. P. Anderson, P. C. Haljan, D. S. Hall, C. E. Wieman, and E. A. Cornell, Phys. Rev. Lett., **83**,

2498 (1999).

[2] K. W. Madison, F. Chevy, W. Wohlleben, and J. Dal-

- ibard, Phys. Rev. Lett., **84**, 806 (2000).
- [3] K. W. Madison, F. Chevy, V. Bretin, and J. Dalibard Phys. Rev. Lett. **86**, 4443 (2001).
- [4] J. R. Abo-Shaer, C. Raman, J. M. Vogels and W. Ketterle, Science **292**, 476 (2001).
- [5] C. Raman, J. R. Abo-Shaer, J. M. Vogels, K. Xu, and W. Ketterle, Phys. Rev. Lett. **87**, 210402 (2001).
- [6] P. C. Haljan, I. Coddington, P. Engels, and E. A. Cornell, Phys. Rev. Lett. **87**, 210403 (2001)
- [7] E. Hodby, G. Hechenblaikner, S. A. Hopkins, O. M. Maragò, and C. J. Foot, Phys. Rev. Lett. **88**, 010405 (2002).
- [8] P. Rosenbusch, D. S. Petrov, S. Sinha, F. Chevy, V. Bretin, Y. Castin, G. Shlyapnikov, and J. Dalibard, Phys. Rev. Lett. **88**, 250403 (2002).
- [9] P. Engels, I. Coddington, P. C. Haljan, V. Schweikhard, and E. A. Cornell Phys. Rev. Lett. **90**, 170405 (2003).
- [10] V. Schweikhard, I. Coddington, P. Engels, V. P. Mogenдорff, and E. A. Cornell, Phys. Rev. Lett. **92**, 040404 (2004).
- [11] I. Coddington, P. C. Haljan, P. Engels, V. Schweikhard, S. Tung, and E. A. Cornell, Phys. Rev. A **70**, 063607 (2004).
- [12] V. Bretin, S. Stock, Y. Seurin, and J. Dalibard, Phys. Rev. Lett. **92**, 050403 (2004).
- [13] S. Stock, V. Bretin, F. Chevy, and J. Dalibard, Europhys. Lett. **65**, 594 (2004).
- [14] V. Bretin, Ph.D. thesis, École Normale Supérieure, 2004.
- [15] A. L. Fetter, Phys. Rev. A **64**, 063608 (2001).
- [16] E. Lundh, Phys. Rev. A **65**, 043604 (2002).
- [17] K. Kasamatsu, M. Tsubota, and M. Ueda, Phys. Rev. A **66**, 053606 (2002).
- [18] G. M. Kavoulakis and G. Baym, New J. Phys. **5**, 51 (2003)
- [19] T. K. Ghosh, Phys. Rev. A **69**, 043606 (2004).
- [20] A. D. Jackson, G. M. Kavoulakis, and E. Lundh, Phys. Rev. A **69**, 053619 (2004).
- [21] E. Lundh, A. Collin, and K.-A. Suominen, Phys. Rev. Lett. **92**, 070401 (2004).
- [22] A. Aftalion and I. Danaila, Phys. Rev. A **69**, 033608 (2004).
- [23] G. M. Kavoulakis, A. D. Jackson, and G. Baym, Phys. Rev. A **70**, 043603 (2004).
- [24] A. L. Fetter, B. Jackson, and S. Stringari, Phys. Rev. A **71**, 013605 (2005).
- [25] T. K. Ghosh, Euro. Phys. J. D **31**, 101 (2004).
- [26] D. E. Sheehy and L. Radzihovsky, Phys. Rev. A **70**, 063620 (2004).
- [27] D. E. Sheehy and L. Radzihovsky, Phys. Rev. A **70**, 051602 (2004).
- [28] A. Aftalion and I. Danaila, Phys. Rev. A **68**, 023603 (2003).
- [29] L.-C. Crasovan, V. M. Pérez-García, I. Danaila, D. Mihalache, and L. Torner, Phys. Rev. A **70**, 033605 (2004).
- [30] A. Aftalion and T. Riviere Phys. Rev. A **64**, 043611 (2001).